E3S Web of Conferences **469**, 00083 (2023) https://doi.org/10.1051/e3sconf/202346900083
ICEGC'2023

Adaptive nonlinear current controller for switched reluctance motor torque ripple optimization

Boumaalif Youness[1,*] and *Ouadi* Hamid[1]

[1]*ERERA, ENSAM, Mohammed V University* in Rabat, Morocco

Abstract. This paper deals with torque ripple minimization in SRM through adaptive nonlinear current control while considering saturation. The proposed methodology for SRM speed tracking is based on Indirect Instantaneous Torque Control (IITC). Optimal references are determined offline using the Particle Swarm Optimization (PSO) algorithm. The optimal current profile is generated by using current sharing function (CSF) block. The nonlinear speed and current controllers are developed using Backstepping technique. The proposed control strategy performance is evaluated using a Matlab Simulink model taking into account the saturation phenomena. The obtained results demonstrate that the adaptation of the control angles as well as the peak current minimizes the torque ripples for different operating conditions.

1 Introduction

With the current technological development, the world is heading towards the depletion of its resources. Thus prompting researchers to find alternatives. The transport field is particularly concerned, where hybrid or electric vehicles represent an optimal solution, despite their high manufacturing cost[1–4]. In order to reduce this cost, a comparative study of existing electric machines has shown that switched reluctance motors (SRM) are the best choice to meet this criterion, while also offering other advantages such as high torque generation, absence of magnets, low rotor inertia, high operating temperature and so on[5–9]. Due to its doubly salient structure, this machine exhibits non linearity in magnetic flux couplings, which results in residual issues like torque ripple, noise, and vibrations.

In the literature, several strategies for reducing torque ripple is proposed. Techniques that rely on modifying the machine's geometry yield satisfactory results for a specific application [10]. However, as soon as operating conditions are modified, this technique shows its limits. Recent research focuses on segmented switched reluctance motor (SSRM), which involves optimizing flux by converting the continuous iron core of the stator/rotor into discontinuous segments insulated by a non-magnetic material [11]. While this solution reduces the coupling of adjacent phase fluxes and base losses, its complex structure, manufacture difficult and high cost postpones its integration in industrial applications like vehicle application . With the development of power electronics, other researchers have chosen advanced control techniques to reduce torque ripple. An efficient current profiling system in both normal and open phase operation is prsented in [12], but it has a high current ripple and variable switching frequency. In [13] a predictive phase current regulator through PWM control is investigated. Because

*e-mail: boumaalif.youness@gmail.com

 https://doi.org/10.1051/e3sconf/202346900083

of the sensitivity to parameters incertainties, the application of this controller is limited. A model predictive current controller with Kalman filter state estimation is purposed [14]. Its drawback that the torque ripple becomes significant especially for high speed values. It has been proven that for high speeds, controllers based only on the current parameter can no longer guarantee good performance. This is due to the influence of the motional electromotive force (EMF), which naturally limits the rate of change of current. Therefore, to achieve low torque ripples at high speeds, the excitation angles θ_{on} and θ_{off} should be optimized.

An improved direct instantaneous torque control of SRM motor drives is proposed in [15]. The excitation angles optimization is completed based on the Multistage Ant Colony algorithm. In [16] a speed control of switched reluctance motor has been etablished using regulation region of switching angle. [17] propose an enhanced direct instantaneous torque control technique based on sliding mode control. Additionally, the hybrid wolf optimization algorithm is used to complete the optimal parameter adaption. Generally, the majority of these works neglect the effect of magnetic saturation. Therefore, the machine performance is limited. In order to take into account the magnetic saturation, the switched reluctance motor equations should be expressed as a function of the current per phase i and the rotor position θ.

In the purpose to minimize torque ripple, more advance methods has been investigated. For example, a new IITC based on torque sharing function (TSF) has been investigated in [18]. The excitation angles and PID controller parameters is optimized by using Flower Pollination Algorithm (FPA). However, this algorithm does not consider EMF voltage effect. In [19], a reference torque neural network online adaptation based on TSF is purposed. Nevertheless, the magnetic saturation phenomena is neglected. It should be mentioned that the performance of this technique is relatively linked to the accuracy of torque to current inversion block, which is generally difficult to achieve.

Based on the above analysis, dealing with torque ripple minimization while considering magnetic saturation is still one of the most challenging control tasks. This motivates us to carry out this study. The major contribution of this work is to establish a novel controller that is intended to meet the following aims:

- Designing an current controller taking into account magnetic saturation;
- Adaptation of excitation angles according to speed and torque variations;
- Generating an optimal reference current profile to reduce torque ripple.

The proposed controller controls the speed with torque ripple optimization. Which consist of two nonlinear speed/current controllers with an optimal reference current profile generation. The nonlinear controllers are investigated based on backstepping technique, using a model that consider magnetic saturation. The optimums peak current (I_p as well as the excitation angles values are carried out based on the PSO algorithm. The reference current profile is generated with the use of torque sharing function (TSF) block. The simulation is carried out based on a SRM 6/4 Matlab model considering the magnetic saturation. The obtained results demonstrate that the adaptation of the control parameters improves the quality of the torque produced for different operating conditions.

This paper is organized as follows: Section 2 presents the problem formulation. The propsed controller design is developed in Section 3. The theoretical analysis results are confirmed by simulation in Section 4. A conclusion and a references list end the paper.

2 Problem formulation

Considering magnetic saturation allows the switched reluctance machine to operate over a wide range of speed and load torque. For this, the SRM equations model should be expressed as a function of the current i and the position θ. In this work a real SRM 6/4 model [20] is considered. Its dynamic equations system is given by:

$$\begin{aligned}\frac{di_x}{dt} &= -a_x \cdot i_x - b_x \cdot i_x \cdot \omega + c_x \cdot u_x \\ \frac{d\omega}{dt} &= -\frac{1}{J} \cdot (f \cdot \omega - T_e + T_L)\end{aligned} \tag{1}$$

Where x = (1,2,3) represent the phase number, u_x is the control signal; i_x the phase current; ω the rotor speed; θ the rotor position; T_e and T_L the electromagnetic and load torque; J the moment of inertia; and f the viscous friction coefficient. The parameters a_x, b_x and c_x are given by:

$$c_x = \left(L_x + i_x \cdot \frac{\partial L_x}{\partial i_x}\right)^{-1}; a_x = c_x \cdot R_x; b_x = c_x \cdot \frac{\partial L_x(\theta, i_x)}{\partial \theta}$$

Where L_x is the phase inductance, R_x is the phase resistance, $\frac{\partial L_x(\theta,i_x)}{\partial\theta}$ and $\frac{\partial L_x(\theta,i_x)}{\partial i_x}$ parameters are the inductance derivatives with respect to θ and i_x respectively. To our knowledge, the approximation of inductance per phase L_x is a challenging task due to its non-linear form in terms of position θ and current per phase i_x. Because of the periodic nature of the inductance profile, it can be approximated by a third-order Fourier transform in order to model periodicity with respect to θ. Moreover, in the purpose to take magnetic saturation into account, harmonic amplitudes ($L_{xj}(i_x)$) are expressed as a function of current per phase by using orthogonal Legendre polynomials. As a result, L_x can be expressed as:

$$\begin{aligned}L_x(\theta, i_x) = L_{x0}(i_x) + L_{x1}(i_x).cos(N_r\theta) + L_{x2}(i_x).cos(2N_r\theta) \\ + L_{x3}(i_x).cos(3N_r\theta)\end{aligned} \tag{2}$$

with $L_{x_i}(i_x) = \sum_{j=0}^{7} a_{xij} P_j(X)$
where N_r represents the rotor teeth number, $P_j(X)$ the j order Legendre polynomial, while X is the normalized current value with respect to the maximum current of the machine with $X = \frac{i_x}{i_{max}}$; and a_{xij} are the optimal coefficients which ensure a better inductance approximation [ref]. Fig.1 shows the inductance form obtained for different excitation currents per phase i_x.

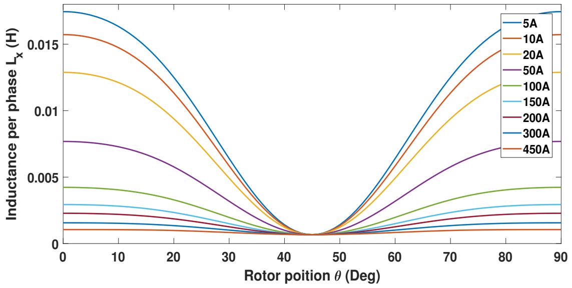

Figure 1: Inductance per phase L_x profile.

On the other hand, the electromagnetic torque expression is provided by:

$$T_e = \sum_{x=1}^{N_{ph}} T_x \tag{3}$$

Where N_{ph} is the SRM phases number and T_x is instantaneous torques par phase which can be expressed as function of the co-energy as:

$$T_x = \frac{\partial}{\partial\theta}\int_0^{i_x}\varphi_x(i_x,\theta)di = \int_0^{i_x}\frac{\partial}{\partial\theta}(L_x(\theta,i).i)di \tag{4}$$

Using equation (2), the derivative of L_x respect to θ, gives:

$$\begin{aligned} T_x &= -N_r\omega\int_0^{i_x}(L_{x1}(i).sin(N_r\theta) + 2.L_{x2}(i).sin(2N_r\theta) \\ &+ 3.L_{x3}(i).sin(3N_r\theta)i.di \\ &= g_{x_1}(i_x).sin(N_r\theta) + 2.g_{x_2}(i_x).sin(2N_r\theta) + 3.g_{x_3}(i_x).sin(3N_r\theta) \end{aligned} \tag{5}$$

where , $g_{xj}(i_x) = -N_r\omega\int_0^{i_x}L_{xj}(i)i.di = \sum_{n=0}^{7} a_{xjn}Q_n(i_x)$
$Q_n(i_x)$: represents the premitive of $P_n(i_x).i_x$ polynom.
Fig.2 depicts the torque per phase profile obtained through this approximation.

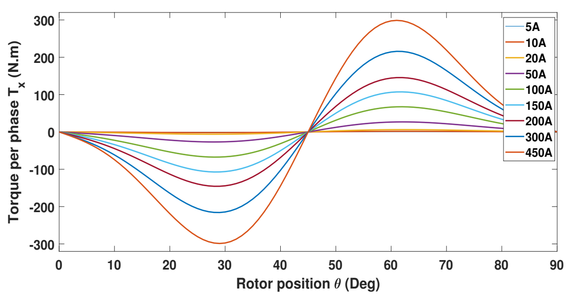

Figure 2: Torque per phase T_x profile.

3 The proposed controller design

3.1 Proposed strategy

For convenience, let remind that we attempt to achieve the following control aims:

- Designing an current controller taking into account magnetic saturation;
- Adaptation of excitation angles according to speed and torque variations;
- Generating an optimal reference current profile to reduce torque ripple.

The proposed control approach in this work employs a modified indirect instantaneous torque control (IITC) technique (see fig.3). It consists of a cascade regulation: outer speed loop and inner current loop, using two nonlinear controllers based on the Backstepping technique. The reference torque T_{ref} generated by the first speed controller is applied to the reference current profile generator block. The latter exploits the table of optimum values of θ_{on}, θ_{off} and I_p, combined with the TSF function to provide the reference current per phase profile i_x^* necessary for the inner current loop in order to produce the corresponding control voltages u_x. The optimums references have been calculated based on metaheuristic method using the PSO algorithm (block that will be developed in the next section). The used power converter drives is an asymmetric half bridge converter [15]. This circuit allows three voltage levels to be applied to the SRM winding: +V, 0, and -V.

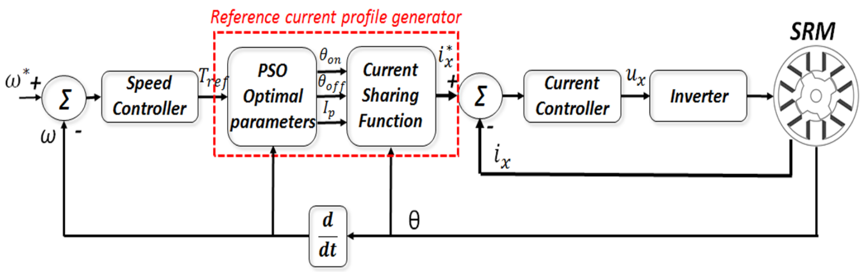

Figure 3: Propoed control method based on IITC technique.

3.2 Reference current profile generator

3.2.1 Optimization problem formulation

By analyzing the torque per phase T_x expression given by(4), we realize that a current control is necessary to generate the desired motor torque. However, for high speed values, the current cannot follow its reference. Hence the need to control the excitation angles. Furthermore, an improper selection of these angles, i.e. during the phase where the inductance variation L_x with respect to θ is negative, produces a negative torque. As a result, torque ripples will increase. On the other hand, due to magnetic saturation, the expression of inductance L_x depends on both the current i_x and the position θ. This means that the zone where $\frac{\partial L_x}{\partial \theta} > 0$ is not fixe. Therefore, controllers using fixed excitation angles do not provide good performance for different machine operating points. Based on the previous discussion, the variables retained in this optimization problem are θ_{on}, θ_{off} and I_p (see fig.4).

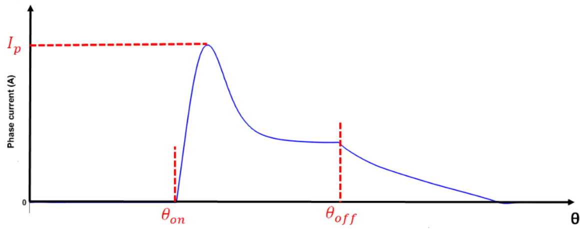

Figure 4: phase current example shape at high speed.

Moreover, torque control techniques acting only on excitation angles and current peak value are usually used with a rectangular current drive. However, only the switching region

 https://doi.org/10.1051/e3sconf/202346900083

time can be defined, while the current dynamics during the switching region is not controlled [21]. Based on this analysis, the dynamic current profile is produced by using a modified sinusoidal torque sharing function (TSF) acting as Current Sharing Function (CSF). Accordingly, this function is given by:

$$\mathrm{i}_{\mathrm{x}}^{*}(\theta) = \begin{cases} 0, & (0 \leq \theta \leq \theta_{on}) \\ \frac{I_p}{2} - \frac{I_p}{2}\cos\frac{\Pi}{\theta_{ov}}(\theta - \theta_{on}), & (\theta_{on} \leq \theta \leq \theta_{on} + \theta_{ov}) \\ I_p, & \left(\theta_{on} + \theta_{ov} \leq \theta \leq \theta_{off}\right) \\ \frac{I_p}{2} + \frac{I_p}{2}\cos\frac{\Pi}{\theta_{ov}}\left(\theta - \theta_{off}\right), & \left(\theta_{off} \leq \theta \leq \theta_{off} + \theta_{ov}\right) \\ 0, & \left(\theta_{off} + \theta_{ov} \leq \theta \leq \theta_{p}\right) \end{cases} \tag{6}$$

with θ_{ov} is overlap angle.

In the purpose to formulate the optimization problem, the dynamic model presented in problem formulation section is adopted. This model exploits the dynamic current (i_x^*) generated by the CSF function to produce the corresponding electromagnetic torque. Thus the objective function is calculated for a given set of variables (θ_{on}, θ_{off} and I_p), operating conditions (measured speed and torque) and constraints.

Due to its ability to further penalize large and prolonged errors, while allowing both the amplitude and the duration of the error to be taken into account. The objective function retained in order to minimize the torque ripples, involves integral quadratic torque error. Which can be represented by the following exrpression:

$$F_{obj} = \sqrt{\frac{1}{\theta_p}\int_0^{\theta_p} \left(T_e(i_x^*, \theta) - T_L\right)^2 d\theta} \tag{7}$$

Using equation (5), the objective function becomes:

$$F_{obj} = \sqrt{\frac{1}{\theta_p}\int_0^{\theta_p} \left(\sum_{x=1}^{N_{ph}}\left(\sum_{j=1}^{3} j.g_{x_j}(i_x^*).sin(jN_r\theta)\right) - T_L\right)^2 d\theta} \tag{8}$$

where θ_p is the electric period.

For a given current profile i_x^*, the dynamic model is used to measures the objective function for each pair of speed and torque. The optimal solution should verifie the constraints imposed. For the SRM 6/4 three phases, the conduction angle should be at least 30° [15]. Moreover, the θ_{off} angle should achieve a maximum exploitation of the zone where $\frac{\partial L_x}{\partial \theta} > 0$ without producing negative torque. Beside, the considered constraints are:

$$\begin{bmatrix} 1 & -1 \\ -1 & 1 \end{bmatrix}\begin{bmatrix} \theta_{on} \\ \theta_{off} \end{bmatrix} < \begin{bmatrix} \frac{-\theta_p}{m} \\ \frac{\theta_p \cdot k}{m} \end{bmatrix} \tag{9}$$

where m represents the number of phases and k is a constant that specifies the upper limit of the excitation angles taken equal to 1.4 [20]. In order to improve the efficiency with less copper loss, a seconde constraint used in this optimization problem conserne the I_{ref} current:

$$I_{ref} \leq 0.8 \cdot I_{max} \tag{10}$$

where I_{max} represents the maximum current supported by the SRM motor.

3.2.2 PSO optimal parameters

Manually tuning the reference current and excitation angles for each speed and torque operating point can be extremely time-consuming. To expedite the tuning process for these parameters, a PSO algorithm is utilized. Mainly chosen for its simplicity, efficiency and assured convergence [22, 23]. The PSO

approach involves particles moving through the problem space with random speeds. They maintain their individual best positions (P_{best}) and associated fitness values, while striving to reach the global best position (G_{best}) that represents the optimal fitness value across the entire search space. At each time step, particles are guided by a weighted random acceleration towards their P_{best} and G_{best} locations. This fundamental concept forms the basis of the PSO approach.
For the operating points retained for this optimization problem, the rotor speed varies from 0 to its nominal value ($200 rad/s$) with a step of $5 rad/s$ while the torque varies from 0 to its nominal value ($300 N.m$) with a step of $10 N.m$. For each setpoint (ω, T), the PSO algorithm continuously explores the θ_{on}, θ_{off} and I_p control parameters to determine the optimal values that improve the quality of the torque produced. To provide further clarification, Fig.5 illustrates a detailed flowchart optimization process of the control parameters. Table 1 summarizes the various parameters used by the PSO algorithm. The optimization problem results are stored offline in a lookup table, as shown in Fig.6. Table 2 gives the statistical analysis of the control variables used.

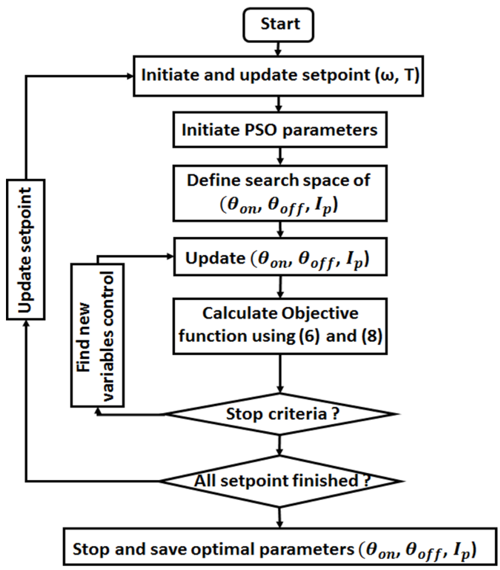

Figure 5: flowchart optimization process of the control parameters

Table 1: PSO Parameters

Parameters	Values
Population size	50
Maximum iteration	30
No. of variable	3
max value of inertia coefficient(ω_{max})	0.9
min value of inertia coefficient (ω_{min})	0.4
acceleration factors (C_1, C_2)	2
Control angle θ_{on} interval	$20° \leq \theta_{on} \leq 60°$
Control angle θ_{off} interval	$60° \leq \theta_{off} \leq 90°$

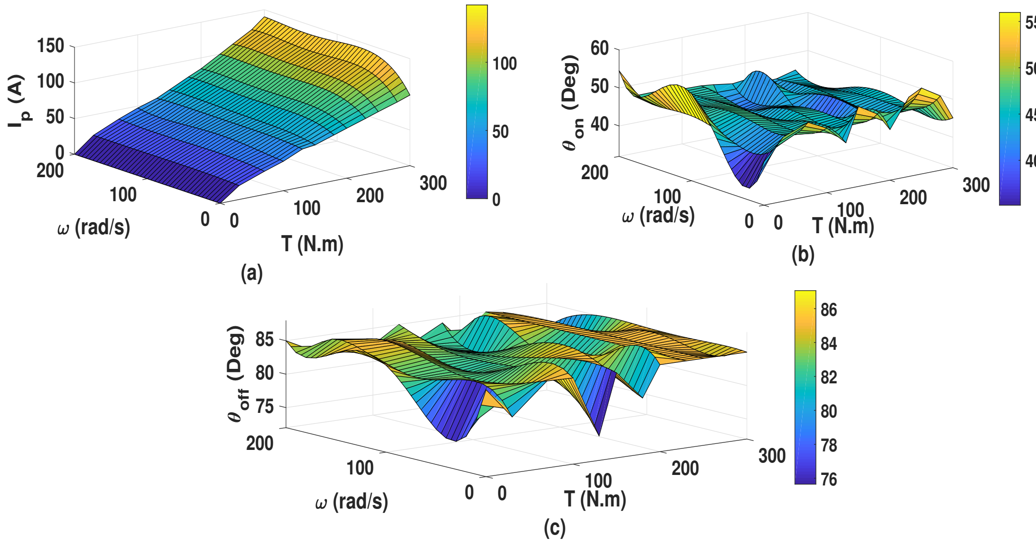

Figure 6: Optimization problem results :(a) current I_p, (b) θ_{on} angle and (c) θ_{off} angle

Table 2: Statistical analysis

Var_name	Average	Median	Std_Deviation	Min	Max
I_p (A)	80.117	83.013	37.556	0	142.03
θ_{on} (Deg)	45.273	45.139	2.7512	35.16	55.971
θ_{off} (Deg)	83.879	84.642	1.7398	75.647	87.062

3.3 Nonlinear speed and current controllers design

As already mentioned in the control strategy section, an instantaneous torque control technique is adopted in this work. In this part the development of nonlinear controllers is completed with the use of the Backstepping technique. The speed controller used in the outer loop aims to provide the torque reference necessary for the inner current loop (see Fig3). The role of the second controller is to force the current to follow the reference (indirect torque control). Consequently, the speed will converge towards its setpoint. Let start by the considered speed and current errors:

$$e_1 = \omega - \omega^* \tag{11}$$

$$z_x = i_x - i_x^*, \quad x = 1, 2, 3 \tag{12}$$

Where ω^* and i_x^* are the speed and current reference signals respectively.
For the speed error e_1, the corresponding Lyapunov functions candidates is given by:

$$V_1 = \frac{1}{2} e_1^2. \tag{13}$$

based on equations (1),(4) and (11) its time dérivative is given by:

$$\dot{V}_1 = \frac{e_1}{J} \cdot (-f \cdot \omega + T_e - T_L - J \cdot \dot{\omega}^*) \tag{14}$$

The deployment of the virtual command T_e such that:

$$T_e = -J \cdot \gamma_1 \cdot e_1 + f \cdot \omega + J \cdot \dot{\omega}^* + T_L \tag{15}$$

Where $\gamma_1 > 0$ is a parameter of the torque controller, gives us:

$$\dot{V}_1 = -\gamma_1 \cdot e_1^2 < 0 \tag{16}$$

But, T_e is not a real control input, so the expression (15) will correspond to the torque reference value.

Remark 3.1 *It should be noted that the torque reference obtained will be converted into a reference current based on the current reference profile generator block. This then makes it possible to develop the current controller.*

On the other hand, for the current error z_x the considered Lyapunov function condidate is given by:

$$V_2 = \sum_x \frac{1}{2} \left(z_x^t \cdot z_x \right) \tag{17}$$

by using equations (1),(4) and (12) its time dérivative is given by:

$$\dot{V}_2 = \sum_x \left[z_x \cdot \left(-a_x \cdot i_x - b_x \cdot i_x \cdot \omega + c_x \cdot u_x - \dot{i}_x^{\,*} \right) \right] \tag{18}$$

Equation (18) allows us to choose the control law u_x such that:

$$u_x = (c_x)^{-1} \cdot \left(-\alpha_x z_x + \dot{i}_x^{\,*} + a_x \cdot i_x + b_x \cdot i_x \cdot \omega \right) \tag{19}$$

Where $\alpha_x > 0$ are the current regulator parameters.
In this case, one has:

$$\dot{V}_2 = -\sum_x \alpha_x \cdot z_x^2 < 0 \tag{20}$$

As a result, we may conclude from equations (16) and (20) that both the speed error e_1 and the current error z_x are globally and asymptotically stable.

4 Simulations results

4.1 Simulation protocol

A simulation was carried out using the SRM 6/4 real model proposed by Matlab, whose different parameters are listed in the Appendix. The simulation protocol adopted in this section consists of three phases. First, the reference speed is set to $100 rad/sec$ with a load of $30 N.m$ (phase A). Then the speed is scaled from $100 rad/sec$ to $200 rad/sec$ while maintaining a charge of $30 N.m$ (Phase B). Finally, at instant 0.15 seconds, the load undergoes a disturbance, going from $30 N.m$ to $70 N.m$ (phase C). Fig.7 show the shape of this protocol.

4.2 Proposed controller validation

In the purpose to demonstrate the effectiveness of the proposed control technique (already presented in fig.3) and based on the control law (15)-(19). The appropriate design parameters are given as follows: $k_1 = 1000$, $c_j = 2400$ with $j = 1, 2, 3$.
Fig.8, Fig.9 and Fig.10 illustrates the speed, torque and phase current results obtained from the proposed controller (PC). It is clear that the suggeted control technique presente efficient speed tracking, even in the presence of a load disturbance, with low torque ripple and low current amplitude despite speed changes. Furthermore, Fig.11 and Fig.12 illustrates how the coresponding optimal control angles adapt faster according to the applied control law. Therefore the SRM machine can achieve high performance. Fig.13 depicts the corresponding peak current variation. It is obvious that the current amplitude remains acceptable. Therefore, copper loses are reduced and the machine efficiency is improved.

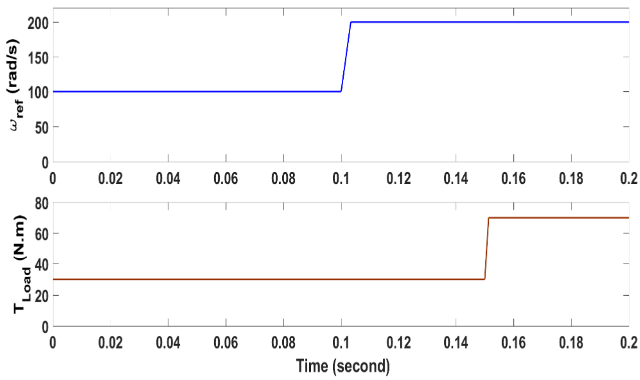

Figure 7: Simulation protocol.

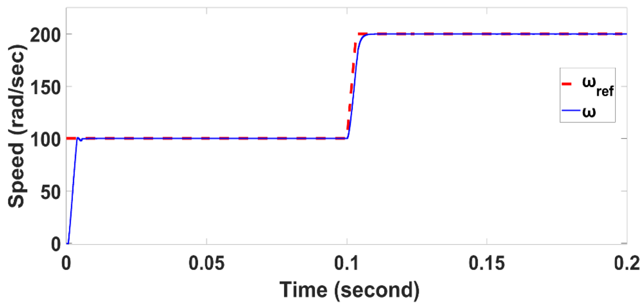

Figure 8: Speed tracking performance.

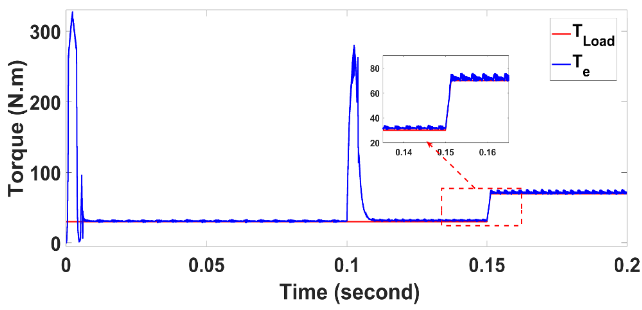

Figure 9: Torque tracking performance.

4.3 Comparative Study

As already mentioned, precise control of both current and excitation angles is crucial for generating the desired motor torque. At high speeds, maintaining accurate current tracking becomes challenging, necessitating control over the excitation angles. Improper selection of these angles, particularly during phases where the variation of inductance with respect to position θ is negative (see Fig.1), results in negative torque and increased ripple. To highlight the importance of adapting the excitation angles, a controller with fixed excitation angles (FEA) is considered for comparison purposes. It consists of a

 https://doi.org/10.1051/e3sconf/202346900083

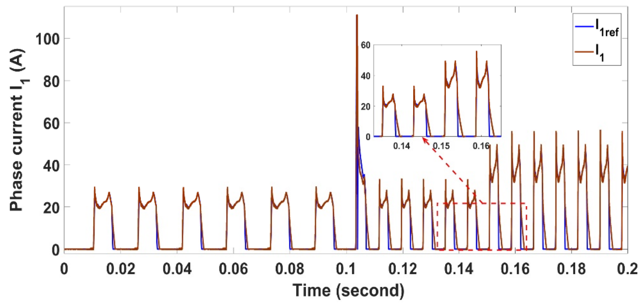

Figure 10: Current profile tracking performance.

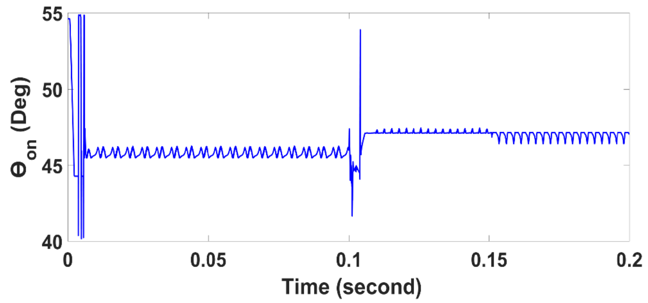

Figure 11: Form of the control angle θ_{on} variation.

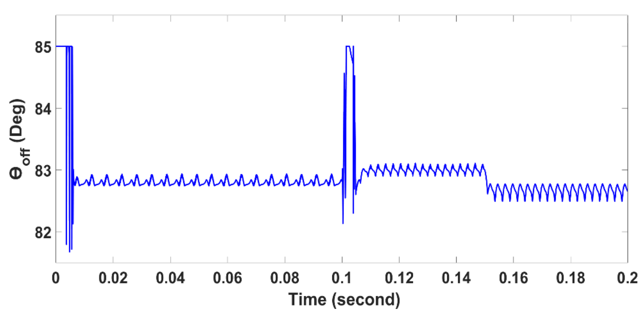

Figure 12: Control angle θ_{off} variation form.

control using the same control law (15)-(19) but with fixed excitation angles ($\theta_{on} = 46°$, $\theta_{off} = 83°$). To give more credibility to our controller, the fixed excitation angles adopted correspond to the optimum values obtained based on the PSO algorithm for a speed of $100 rad/sec$ and a load torque of $30 N.m$.

Moreover, we have already mentioned that rectangular current controllers manipulate excitation angles and peak current values. However, these methods are limited to determining the duration of the switching zone, without guaranteeing dynamics current control during this period. For comparison purpose and to emphasize the importance of controlling the current dynamics during this phase, a second controller using a rectangular current profile (RCP) is considered.
Fig.14, Fig.15 and Fig.16 show the shapes of speed, torque and current per phase respectively obtained

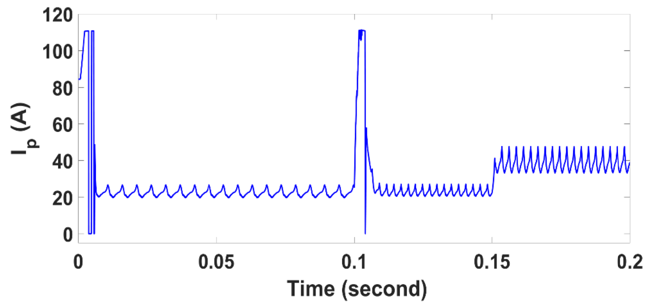

Figure 13: Shape of the peak current I_p variation.

for the both controllers when applying the same simulation protocol as depicted before. It is evident that both controllers provides speed tracking with low torque ripple for speeds of $100 rad/sec$. However, for a speed of $200 rad/s$, it is clearly observed that the torque ripples have increased significantly specially during torque load disturbance especially for the FEA controller. This demonstrates the need for adaptation. Furthermore, the obtained phase current amplitudes are significant for the FEA controller, which reduces the machine efficiency. Moreover, the RCP controller accurately tracks its reference between the moments when the excitation angles are applied, but it does not effectively control the current dynamics during this period. As a result, significant torque ripples occur during the transition phase. For more details, Table 3 summarizes this comparison. Where I_{1rms}, ΔI_1 and T.ripple represent the RMS current per phase value, the current ripple and the torque ripples respectively. These values are calculated based on the following equations:

$$I_{1rm} = \sqrt{\frac{1}{\theta_p}\int_0^{\theta_p} I_1^2 d\theta}$$

$$\Delta I_1(\%) = \frac{I_{1max} - I_{1ave}}{I_{1mean}} \times 100$$

$$T_{ripple}(\%) = \frac{T_{emax} - T_{emin}}{T_{eave}} \times 100$$

It should be noted that this table is generated based on 100 tests, and these values correspond to the average measurements.

Thus, the propesed controller provides speed tracking with low torque ripple and low current amplitude. These findings reinforce the effectiveness of the control strategy and suggest that it can be successfully utilized across various machine operating points.

Table 3: Comparative results between controllers

Operating condition	Phase A			Phase B			Phase C		
Metrics	FEA	RCP	PC	FEA	RCP	PC	FEA	RCP	PC
I_{1rms} (A)	19.63	15.38	15	18.77	16.59	15.83	36.39	26.23	23.14
ΔI_1 (%)	178.97	18.82	21.6	70.35	15.52	23.24	107.44	18.37	29.45
T.ripple (%)	39.9	25	13.15	73.62	34.04	11.69	62.74	35.78	9.71

5 Conclusion

To improve the torque quality, an adaptive nonlinear current controller has been developed while considering magnetic saturation. Moreover, the optimal controller parameters has been carried out by using

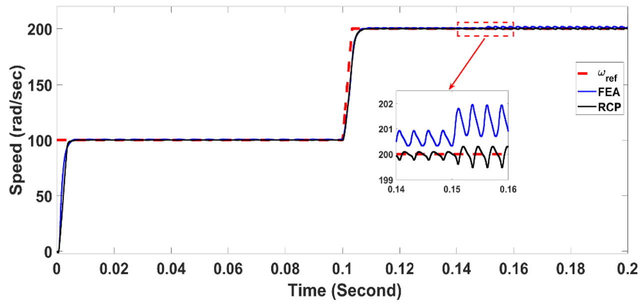

Figure 14: Conventional controllers speed shape under the same control law

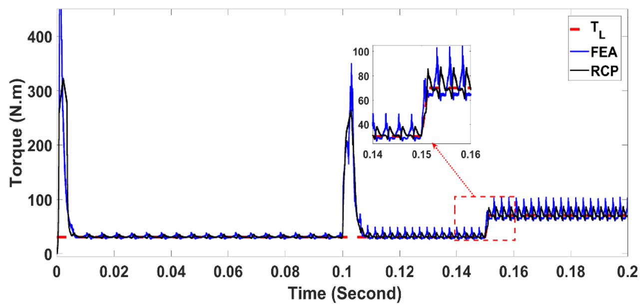

Figure 15: Conventional controllers torque form under the same control law.

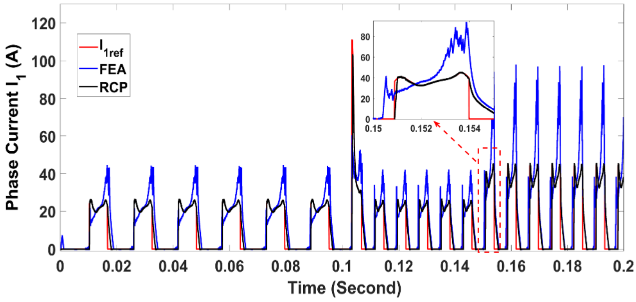

Figure 16: Conventional controllers current shape under the same control law.

PSO algorithm. The reference current profil has been generated by using current sharing function, which eliminates the torque to current bloc inversion. Based on a SRM 6/4 Matlab model taking into account magnetic saturation, the simulation outcomes has been acheived. The obtained results demonstrate the performance of the proposed controller, whether it is for controlling with fixed excitation angles (FEA) or for the controller using a rectangular current profile (RCP). Especially when dealing with sudden load variations while guaranteeing a speed error that does not exceed $10^{-3} rad/s$ and with torque ripples three times lower than both controllers. Moreover, the phase current amplitude also controlled, which guarantees an improvement in the machine efficiency.

Acknowledgment

This work was supported by the Ministry of Higher Education, Scientific Research and Innovation, the Digital Development Agency (DDA) and the CNRST of Morocco (Alkhawarizmi/2020/39).

Appendix

Table 4: Table of the SRM 6/4 features

Parameters	Value
Stator poles/Rotor polest	$\frac{6}{4}$
Number of phases	3
Max Power	60 kW
Bus Voltage	240 V
Phase winding resistance	0.05Ω
Maximal phase current	450 A
Maximal phase flux linkage	0.486 Wb
Rotor friction	0.01 $N.m.s$
Rotor inertia	0.0082 $Kg.m^2$
Saturated aligned inductance	0.15 (mH)
Aligned inductance	23.6 (mH)
Unaligned inductance	0.67 (mH)

References

[1] G. Fang, F.P. Scalcon, D. Xiao, R.P. Vieira, H.A. Gründling, A. Emadi, IEEE Open Journal of the Industrial Electronics Society **2**, 280 (2021)
[2] A. EL AOUMARI, H. Ouadi, International Journal of Renewable Energy Research (IJRER) **11**, 1639 (2021)
[3] J. El-bakkouri, H. Ouadi, F. Giri, A. Saad, Proceedings of the Institution of Mechanical Engineers, Part D: Journal of Automobile Engineering p. 09544070221140938 (2022)
[4] H. Ouadi, A. Aitchihab, F. Giri, Journal of Control, Automation and Electrical Systems **31**, 726 (2020)
[5] I. Boldea, CES Trans. Electr. Mach. Syst. **1**, 3 (2017)
[6] S. Gheouany, H. Ouadi, F. Giri, S. El Bakali, Energy Conversion and Management **291**, 117309 (2023)
[7] N. Mounir, H. Ouadi, I. Jrhilifa, Energy and Buildings **288**, 113022 (2023)
[8] H. Ouadi, F. Giri, L. Dugard, International Journal of Modelling, Identification and Control **14**, 27 (2011)
[9] S. Gheouany, H. Ouadi, F. Giri, S. El Bakali, Energy Conversion and Management **291**, 117309 (2023)
[10] K.M. Rahman, S.E. Schulz, IEEE Trans. Ind. Appl. **38**, 1500 (2002)
[11] Z. Xu, T. Li, F. Zhang, Y. Zhang, D.H. Lee, J.W. Ahn, Energies **15**, 9212 (2022)
[12] P. Dúbravka, P. Rafajdus, P. Makyš, L. Szabó, IET Electric Power Applications **11**, 548 (2017)

[13] S. Shen, H. Wang, Y. Feng, M. Li, Y. Zhong, Applied Sciences **12**, 1688 (2022)
[14] X. Li, P. Shamsi, IEEE transactions on Industrial Electronics **63**, 3934 (2015)
[15] F. Al-Amyal, L. Számel, M. Hamouda, Ain Shams Engineering Journal **14**, 101967 (2023)
[16] Y. Zhang, L. Chen, Z. Wang, E. Hou, Energies **15**, 5782 (2022)
[17] Z. Jin, X. Sun, G. Lei, Y. Guo, J. Zhu, IEEE Transactions on Industrial Electronics **69**, 4534 (2021)
[18] M. Gengaraj, L. Kalaivani, R. Rajesh, IETE Journal of Research pp. 1–15 (2022)
[19] B. Jing, X. Dang, Z. Liu, J. Ji, Machines **11**, 179 (2023)
[20] Y. Boumaalif, H. Ouadi, International Journal of Power Electronics and Drive Systems **14**, 77 (2023)
[21] Y. Boumaalif, H. Ouadi, IFAC-PapersOnLine **55**, 240 (2022)
[22] S. El Bakali, O. Hamid, S. Gheouany, Clean Energy **7**, 911 (2023)
[23] S. Gheouany, H. Ouadi, S. El Bakali, Clean Energy **7**, 375 (2023)